LES of Laser ignition in a micro-combustor

G. Lacaze, B. Cuenot

CERFACS, 31057 Toulouse, France

T. Poinsot

IMFT, 31400 Toulouse, France

CERFACS has applied the LES code AVBP to the test case 4 of the 3rd International Workshop on Rocket Combustion Modelling. In this configuration the M3 micro-combustor installed at DLR is filled with separate H2 and O2 streams at a global equivalence ratio of 4, and then ignited by a Laser beam. The resulting H2/O2 ignition kernel, flame propagation and stabilisation are observed in the simulation and compared to experimental images. Results show that the simulation captures the main mechanisms of ignition and combustion in this particular configuration.

I.   Introduction

Large Eddy Simulation (LES) is a powerfull tool for the numerical study of unsteady complex flows. The concept of explicitely solving for the large geometry-dependent turbulent scales while modelling the dissipative behavior of the smaller scales, combined with high order numerical schemes and optimized unstructured meshes, has already shown its high potential on gaseous turbulent flows.[1–4] Its recent extension to reacting flows confirmed this potential and led to very new and helpful results.[5–10] Application of LES to the highly compressible and reacting flows that appear in rocket engines is therefore a natural evolution of this method.[11]

In the last years CERFACS in collaboration with IFP has developed a numerical tool (AVBP) devoted to the LES of reacting flows in gas turbines and piston engines geometries. It is used here to compute the RCM test case 4, i.e. the laser ignition of gaseous O2/H2 in the M3 micro-combustor installed at DLR.[12] The test case is a good candidate for LES application as ignition and flame stabilisation are transient phenomena that require accurate discretisation and modelling. It corresponds to the case GGA 24, at a global stoichiometry of 4 and with a chamber length of 140 mm. The pressure and temperature in the dome of oxygen are 11.7 bars and 300K and the oxygen mass flow rate is 1.135g/s . If the injection of oxygen is supposed sonic (no acoustic feedback is observed), it is possible to evaluate the pressure loss between the dome and the chamber inlet, allowing to estimate the pressure and temperature of the injected oxygen at respectively 2.5 bars and 356K. This leads to an inlet velocity of 370 m/s (Mach = 1). Pressure loss in the hydrogen line is not so important and hydrogen is injected at the dome temperature of 302K. The mass flow rate is 0.592 g/s, corresponding to a velocity of 376 m/s and a subsonic Mach number of 0.28. Ignition occurs after a long (370 ms) filling phase during which the nitrogen initially in the chamber is gradually replaced by H2 and O2 at a global stoichiometry of 4. This raises several questions:

- Is there nitrogen left in the chamber at the time of ignition?

- How efficient is the mixing between hydrogen and oxygen?

- What is the flow structure?

Before starting the full 3D LES of the chamber, it is helpful to perform simple 0D calculations to better understand the conditions in which ignition occurs. Figure 1 shows the pressure rise given by a 0D constant volume calculation, considering the mixture in equilibrium state and including the mass flow rate leaving the volume through the exit nozzle. This calculation does not include Nitrogen, assuming that it has all left the volume at ignition. Compared to the experimental pressure curve, the 0D calculation surprisingly gives very pertinent results. This means that although not infinitely fast, the chemichal process is still very fast and that the reactants are well mixed in the ignition and reaction zones during the flame development.
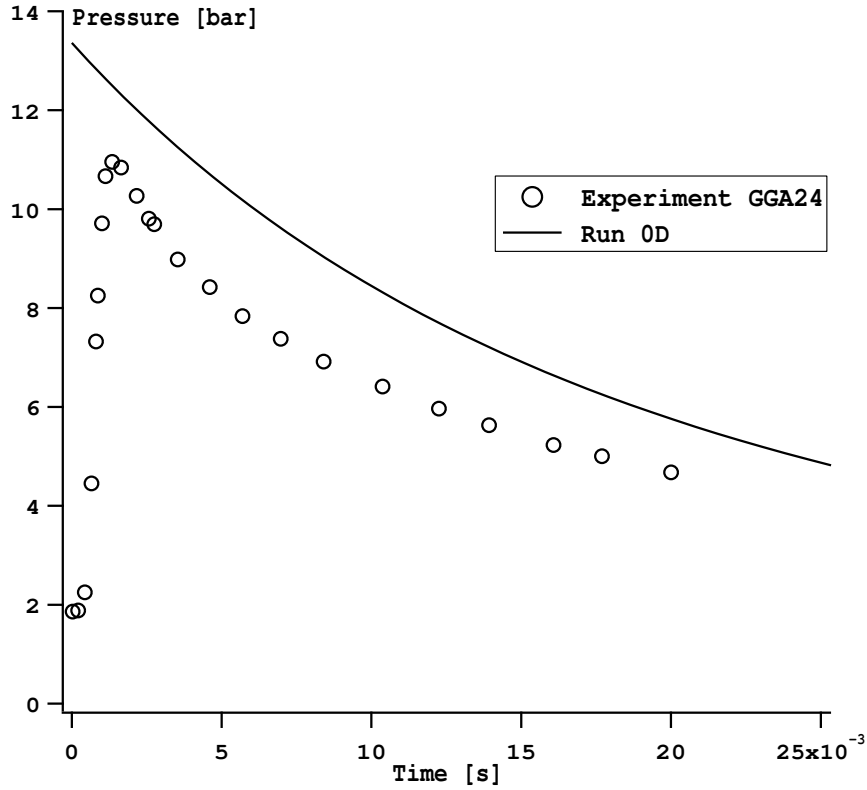
Figure 1. Pressure rise from a 0D equilibrium calculation, without N2.

II.   Numerical approach

In the mathematical description of compressible turbulent flows with chemical reactions and species transport, the primary variables are the species volumic mass fractions $\rho_\alpha(\mathbf{x}, t)$, the velocity vector $u_i(\mathbf{x}, t)$, the total energy $E(\mathbf{x}, t) \equiv e_s + 1/2 \ u_i u_i$, and the density $\rho(\mathbf{x}, t) = \sum_{\alpha=1}^{N} \rho_\alpha(\mathbf{x}, t)$. Note that $\rho_\alpha(\mathbf{x}, t)$ is linked to the species mass fractions $Y_\alpha(\mathbf{x}, t)$ for which mass conservation imposes for a mixture of N species: $\sum_{\alpha=1}^{N} Y_\alpha(\mathbf{x}, t) = 1$.

The fluid to be considered follows the ideal gas law, $p = \rho \, r \, T$ and $e_s = \int_0^T C_p \, dT - p/\rho$, where e_s is the mixture sensible energy, T the temperature, C_p the fluid heat capacity at constant pressure and r is the mixture gas constant. The viscous stress tensor, the heat diffusion vector and the species molecular transport use classical gradient approaches. The fluid viscosity follows Sutherland's law, the heat diffusion coefficient follows Fourier's law, and the species diffusion coefficients are obtained using a species Schmidt number along with the Hirschfelder Curtis approximation. Note that due to this last approximation, diffusion velocity corrections are added for mass conservation. The application of the LES filtering operation to the instantaneous set of compressible Navier-Stokes transport equations with chemical reactions yields the LES transport equations to be solved numerically,[13] where the non-linear Sub-Grid Scale (SGS) quantities are modelled.[14, 15]

A.   LES closures

The problem of unresolved SGS stress tensor $\overline{\tau_{ij}}^t$, is usually addressed through the concept of SGS turbulent viscosity model and the Boussinesq assumption.[16, 17] The model henceforth reads:

$$\overline{\tau_{ij}}^t - \frac{1}{3} \overline{\tau_{kk}}^t \delta_{ij} = -2 \, \overline{\rho} \, \nu_t \, \widetilde{S}_{ij}, \tag{1}$$

with

$$\widetilde{S}_{ij} = \frac{1}{2}\left(\frac{\partial \widetilde{u}_i}{\partial x_j} + \frac{\partial \widetilde{u}_j}{\partial x_i}\right) - \frac{1}{3}\frac{\partial \widetilde{u}_k}{\partial x_k}\,\delta_{ij}. \tag{2}$$

In Eqs. (1) and (2) $\widetilde{S}_{ij}$ is the resolved strain tensor and ν_t is the SGS turbulent viscosity. The Smagorinsky model[18] is used here. It expresses ν_t as:

$$\nu_t = (C_S \triangle)^2\,\|S\|. \tag{3}$$

In Eq. (3), $\triangle$ denotes the filter characteristic length and is approximated by the cubic-root of the cell volume, C_S is the model constant ($C_S = 0.18$) and $\|S\| = (2\,\widetilde{S}_{ij}\widetilde{S}_{ij})^{1/2}$.

The SGS species flux $\overline{J_i^\alpha}^t$ and the SGS energy flux $\overline{q_i}^t$ are respectively modelled by use of the species SGS turbulent diffusivity $D_t^\alpha = \nu_t/Sc_t^\alpha$, where Sc_t^α is the turbulent Schmidt number ($Sc_t^\alpha = 0.7$ for all α). The eddy diffusivity is also used along with a turbulent Prandtl number $Pr_t = 0.9$, so that $\lambda_t = \overline{\rho}\,\nu_t\,C_p/Pr_t$:

$$\overline{J_i^\alpha}^t = -\overline{\rho}\left(D_t^\alpha\,\frac{W_\alpha}{W}\,\frac{\partial \widetilde{X}_\alpha}{\partial x_i} - \widetilde{Y}_\alpha\,V_i^c\right) \quad \text{and} \quad \overline{q_i}^t = -\lambda_t\,\frac{\partial \widetilde{T}}{\partial x_i} + \sum_{\alpha=1}^{N}\overline{J_i^\alpha}^t\,\widetilde{h}_s^\alpha. \tag{4}$$

In Eq. (4) the mixture molecular weight W and the species molecular weight W_α can be combined with the species mass fraction to calculate the molar fraction of species α: $X_\alpha = Y_\alpha W/W_\alpha$. In expression (4), V_i^c is the diffusion correction velocity resulting from the Hirschfelder-Curtis approximation[13] and $\widetilde{T}$ is the modified filtered temperature which satisfies the modified filtered state equation,[1,19–21] $\overline{p} = \overline{\rho}\,r\,\widetilde{T}$. Finally, $\widetilde{h}_s^\alpha$ stands for the enthalpy of species α.

The modelling of SGS combustion terms is based on the "thickened flame" model. Following the theory of laminar premixed flames[26] the flame speed S_L^0 and the flame thickness δ_L^0 may be expressed as:

$$S_L^0 \propto \sqrt{\lambda A} \quad \text{and} \quad \delta_L^0 \propto \frac{\lambda}{S_L^0} = \sqrt{\frac{\lambda}{A}}, \tag{5}$$

where λ is the thermal diffusivity and A the pre-exponential constant. Increasing the thermal diffusivity by a factor F, the flame speed is kept unchanged if the pre-exponential factor is decreased by the same factor. In this operation the flame thickness is multiplied by F and easily resolved on a coarser mesh. For accurate mixing predictions, dynamic thickening is introduced to avoid overestimation of molecular and thermal diffusion in partially mixed zones where no combustion occurs.[13] The interaction between turbulence and chemistry is modelled through the the so-called efficiency function, E.[27] The final expressions of the SGS combustion models read:

$$\overline{J_i^\alpha}^t = (1-S)\,\overline{\rho}D_t^\alpha\,\frac{W_\alpha}{W}\,\frac{\partial \widetilde{X}_\alpha}{\partial x_i} + \overline{\rho}\,\widetilde{Y}_\alpha\,V_i^c \quad \text{and} \quad \overline{q_i}^t = (1-S)\,\lambda_t\,\frac{\partial \widetilde{T}}{\partial x_i} + \sum_{\alpha=1}^{N}\overline{J_i^\alpha}^t\,\widetilde{h}_s^\alpha. \tag{6}$$

where V_i^c is obtained as usual and includes the correction coefficient $(1-S)$. In Eq. (6), S is the local sensor depending on the local temperature and mass fractions.

III. Numerical configuration and simulation

The LES code AVBP solves the filtered Navier-Stokes conservation equations on unstructured meshes, using a finite volume formulation and explicit integration schemes. Realistic thermochemistry is used, allowing multi-step kinetics for the oxidation of hydrocarbons or hydrogen. Boundary conditions are set with the NSCBC method[28] based on characteristic variables. All simulations presented in this paper are run with the second-order Lax-Wendroff scheme.

The numerical configuration reproduces the 3D combustion chamber with the H2 and O2 inlet tubes and the exit throat. The injection systems with the domes are not included in the simulation. To minimize the impact of boundary condition at the exit, the ambient atmosphere is also calculated on a coarse mesh added to the chamber exit. The mesh is refined around the jets at inlet and downwards where the jets mix, develop and are ignited. The configuration and a zoom of the mesh near the injections are represented on Fig. 2. The final mesh is fully unstructured and uses tetrahedral cells. It counts around 630000 nodes, with the smallest cell volume being of the order of 10^{-13} m^3. At inlet the momentum, temperature and mass

fractions are imposed, whereas the exit surface (which is located outside the chamber, in the free atmosphere) is relaxed to the ambient pressure. All solid boundaries are isothermal slip walls, at the temperature 300K. The one-step chemistry is represented by the irreversible reaction $H_2 + 0.5\ O_2 \rightarrow H_2O$ with an Arrhénius law $\dot{\omega} = A[H_2][O_2]^{1/2}exp(-E/kT)$ with $A = 5.4\ 10^{12}$ and $E = 34500cal/mol$. Laser ignition is reproduced through an energy deposition at the location of the laser beam impact. The complex physical and chemical phenomena that are induced by the laser beam are not simulated. In particular an important part of the laser energy is very rapidly dissipated. The computation only takes into account the resulting effective energy input to the gas, estimated at 35 mJ for 10^{-7}s, spread over a 6mm diameter sphere.

IV. Results

A. The filling phase

Although the 0D calculation presented in section I shows that segregation has little effect on the pressure curve, it is necessary to establish the correct flow structure and reactants distribution to capture the flame ignition and stabilisation mechanisms. To this purpose a 3D LES of the filling of the chamber initially filled with N2 was performed. With a time step of the order of 8.9 10^{-8}s, the simulation of the 370 ms of the filling phase requires about 10^5 iterations. To spare computing time, the simulation was run on a coarse mesh for 369 ms (118 hours on 16 processors of Cray XD1) and only the last ms, corresponding to two acoustics times, was run on the fine mesh described above (26 hours on 128 processors of the SGI 3800 at CINES). The instantaneous axial velocity field obtained at the end of the filling phase in the median cutting plane is shown on Fig. 3 with a 0-velocity isocontour superimposed. This indicates the location of recirculation zones starting at the corners of the chamber and developing downwards around the jets. Figures 5, 4 and 6 show in the same cutting plane the fields of N2, O2 and equivalence ratio obtained at 370 ms. It appears that effectively nearly all the nitrogen has been purged, as confirmed by the time evolution of the total N2 in the chamber given on Fig. 7. The remaining N2, mostly trapped in the recirculation zones, has a maximum mass fraction of the order of 0.17. The reactants are well mixed in most part of the chamber, segregation appears only in the vicinity of the inlet jets, where their vortical structure is clearly visible. The associated pressure field (Fig. 8) allows to identify the succession of compression/expansion cells typical of sonic jets. The transverse oxygen profiles obtained at the end of the filling phase ($t = 370$ms) are shown at three different axial positions on Fig. 9. The comparison with the Rayleigh intensity measurements shown on Fig. 10 is satisfactory: although the direct quantitative comparison is not possible as the Rayleigh intensity profiles have not been rescaled, the shape of the curves is well recovered by the simulation, with a correct peak thickness and maximum value.

B. Ignition

The solution obtained at 370 ms is then ignited with an energy deposition as explained in section III. Figures 11, 12 and 13 show series of snapshots of the fields of temperature, reaction rate, and H2 at four different times ($t = 15, 103, 226, 684\mu s$ after ignition). Schlieren photographs taken at $35, 250$ and $680\mu s$ after ignition are also shown on Fig. 11. The comparison clearly shows that the simulation captures the correct flame behavior as the global flame shapes are well recovered by the computation at the correct times. These images illustrate clearly the flame ignition and propagation towards the walls, the exit and the injection. A flame kernel forms immediately at the energy deposition zone, and the temperature rises to a value exceeding the flame temperature, reaching a maximum of 4124K. This is due to the energy deposition that mimics the laser beam. In reality the maximum temperature increases locally to even higher values, inducing complex chemical phenomena. These can not be captured with the model used in this simulation, but these phenomena are very brief and the temperature decreases very rapidly after the end of the energy deposition, reaching a state close to the one observed in the simulation.

The laser beam impact is located in a segregated zone where the local stoichiometric ratio is around 2. As the flame expands in all directions, it encounters mixtures with different stoichiometric ratio: the front propagating towards the walls and the exit burns a mixture at $\Phi = 4$ but the front propagating towards the injection jets sees more and more segregated reactants. At $t \approx 200\mu s$ part of the upward propagating flame front encounters a mixture close to stoichiometry and accelerates. In the same time the pressure starts rising, untill the flame reaches the walls and burns the fuel trapped between the flame front and the wall. At $t = 684\mu s$ the chamber is almost completely filled with burnt gas and a partially premixed flame starts to

establish near the injection. After complete burning of the fuel trapped near the walls, the premixed flame will extinguish in this zone and only the flame stabilised at the injectors will remain. This last phase has not been simulated yet and will be shown in a future paper.

The corresponding pressure rise is plotted in Fig 14 and compared to the experimental curve. The computed pressure starts to increase at a correct time but then increases too fast, due to the use of a simple one-step chemistry kinetics model, known to perform poorly on ignition problems: the lack of induction chemical mechanisms leads to an exponential rise of the reaction rate after the ignition temperature is passed. The use of an optimized chemical scheme including more species will improve this result and will also be presented in a future paper.

V.   Conclusion

A first attempt to apply Large eddy simulation to test case 4 of the RCM workshop, corresponding to the laser ignition of the M3 burner of DLR has been presented. Results are qualitatively in good agreement with experimental observations, showing that the simulation captures the right mechanisms for flame propagation and stabilisation. As the simulation used only one-step chemistry, the pressure rise associated with the flame ignition and expansion is too fast but starts at the correct time. It may be concluded that the flow and flame structure are now better understood and that complex chemistry simulations can be started to allow a full and quantitative validation.

Acknowledgments

References

[1] P. Moin, K. Squires, W. Cabot, and S. Lee, *A dynamic subgrid-scale model for compressible turbulence and scalar transport*, Physics of Fluids, **3**, 11, pp.2746-2757, 1991.

[2] M. Lesieur and O. Metais, *New Trends in Large-Eddy Simulations of Turbulence*, Annual Review of Fluid Mechanics, **28**, pp. 45-82, 1996.

[3] M. Lesieur and P. Comte, *Large-Eddy Simulations of Compressible Turbulent Flows*, Turbulence in Compressible Flows, pp. 4.1-4.39, 1997.

[4] Garnier E., Sagaut P. and Deville M., *Large Eddy simulation of shock/homogeneous turbulence interaction*, Computers and Fluids, **31**, 2, pp. 245-268, 2002.

[5] L. Selle *et al.*, *Compressible Large-Eddy Simulation of turbulent combustion in complex geometry on unstructured meshes*, Combustion and Flame, **137**, 4, pp.489–505, 2004.

[6] S. Roux *et al.*, *Studies of mean and unsteady flow in a swirled combustor using experiments, acoustic analysis and Large Eddy Simulations*, Combustion and Flame, in press, 2005.

[7] V. Sankaran *et al.*, *LES of Spray Combustion in Swirling Flows*, Journal of Turbulence, Vol. 3, No 2, 2002.

[8] H. Pitsch *et al.*, *Flamelet modeling of non-premixed turbulent combustion with local extinction and re-ignition*, Comb. Theory Modelling, 2002.

[9] Y. Sommerer *et al.*, *Large eddy simulation and experimental study of flashback and blow-off in a lean partially premixed swirled burner*, Journal of Turbulence, 5:037, 2004.

[10] C. Prire *et al.*, *Experimental and numerical studies of dilution systems for low emission combustors*. AIAA Journal, 43(8):1753-1766, 2005.

[11] , A. Dauptain, *Allumage des moteurs fusée cryotechniques*, PhD thesis, INPT, CERFACS, 2006.

[12] V. Schmidt, U. Wepler, O. Haidn and M. Oschwald, *Characterization of the Primary Ignition Process of a Coaxial GH2/LOX Spray*, AIAA-2004-1167, 42nd AIAA Aerospace Sciences Meeting and Exhibit, Reno, Nevada, 2004.

[13] Poinsot, T. *et al..*, *Theorical and Numerical Combustion*, R. T. Edwards, 2001.

[14] Ferziger, J. H., *Large eddy simulations of turbulent flows*, AIAA Journal, Vol. 15, No. 9, pp. 1261-1267, 1977.

[15] Sagaut, P., *Large Eddy Simulation for incompressible flows,* New York, Springer, 2001.

[16] Pope, S. B., *Turbulent Flows,* Cambridge, UK, Cambridge University Press, 2000.

[17] Chassaing, P., *Turbulence en Mécanique des fluides. Analyse du phénomène en vue de sa modélisation à l'usage de l'ingénieur*, Toulouse, Polytech, 2000.

[18] Smagorinsky, J., *General recirculation experiments with the primitive equations. I. The basic experiment*, Monthly Weather Review, Vol. 91(3), pp. 99-164, 1963.

[19] Erlebracher, G.*et al.*, *Towards the large eddy simulation of turbulent flows*, Physics of Fluids, Vol. 238, pp. 155, 1992.

[20]Ducros, F.*et al.*, *Large-eddy simulation of transition to turbulence in a boundary layer over an adiabatic flat plate*, Journal of Fluid Mechanics, Vol. 326, 1996, pp. 1-36, 1996.

[21]Comte, P.*et al.*, *New tools in Turbulence Modelling. Vortices in incompressible LES and non-trivial geometries*, Course of Ecole de Physique des Houches, Springer-Verlag, France, 1996.

[22]Lilly, D. K., *A proposed modification of the germano sub-grid closure method*, Physics of Fluids, Vol. A4, 3, pp. 633-635, 1992.

[23]Germano, M., *Turbulence: The filtering approach*, Journal of Fluid Mechanics, Vol. 238, pp. 238-325, 1992.

[24]Meneveau, C. *et al.*, *A lagrangian dynamic subgrid-scale model of turbulence*, Journal of Fluid Mechanics, Vol. 319, pp. 353-385, 1996.

[25]Ghosal, S. *et al.*, *A dynamic localization model for large eddy simulation of turbulent flow*, Journal of Fluid Mechanics, Vol. 286, pp. 229-255, 1995.

[26]Williams, F. A., *Combustion theory*, New-York, Benjamin Cummings, 1985.

[27]O. Colin *et al.*, *A thickened flame model for Large Eddy Simulations of turbulent premixed combustion*, Physics of Fluids, 12(7):1843-1863, 2000.

[28]T. Poinsot and S. Lele, *Boundary conditions for direct simulations of compressible viscous flows*, Journal of Computational Physics, **101**, 1, pp.104-129, 1992.
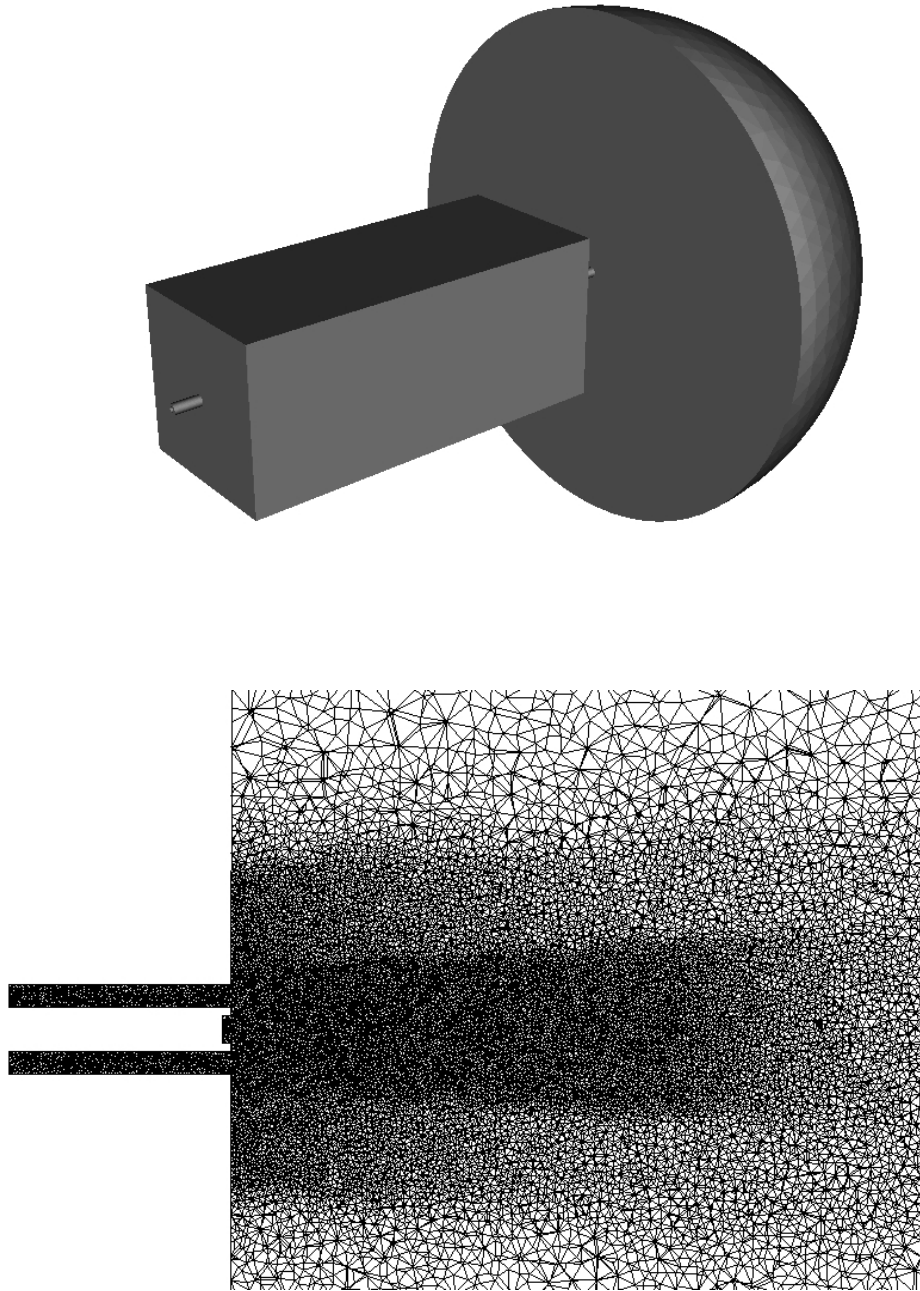
Figure 2. View of the computing domain and zoom of the mesh of the M3 micro-combustor.

velocity[X]

7.477e+02
5.320e+02
3.162e+02
1.004e+02
-1.154e+02
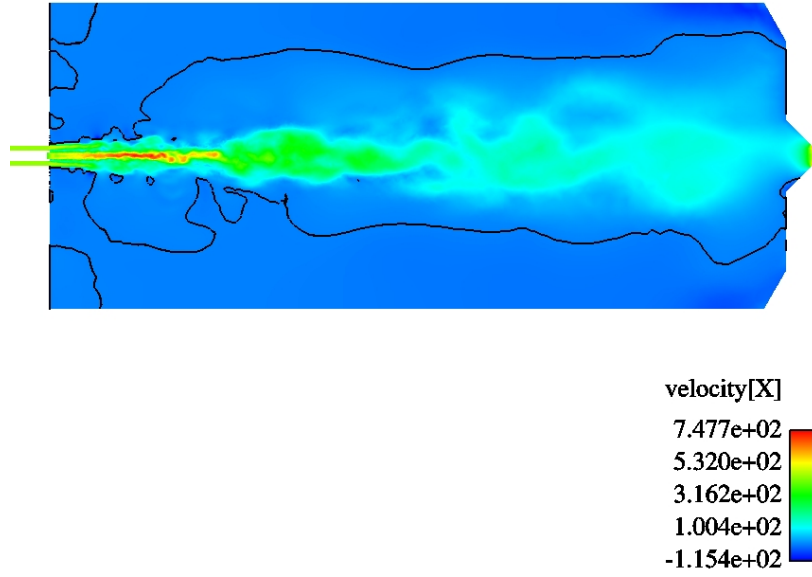
Figure 3. Axial velocity and 0-isocontour at t=370 ms.

Y_O2

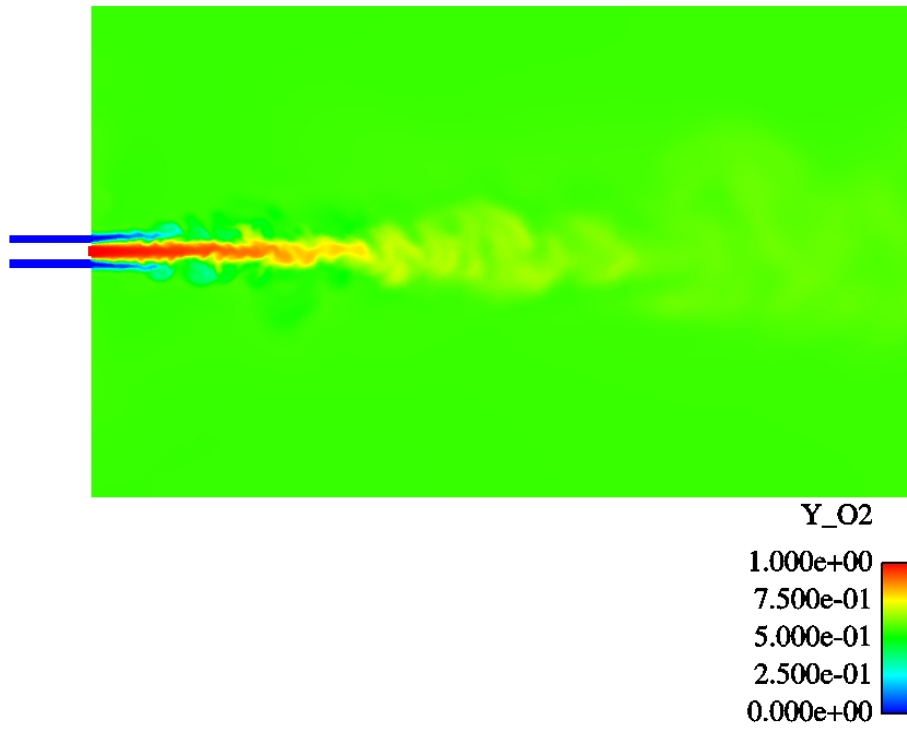1.000e+00
7.500e-01
5.000e-01
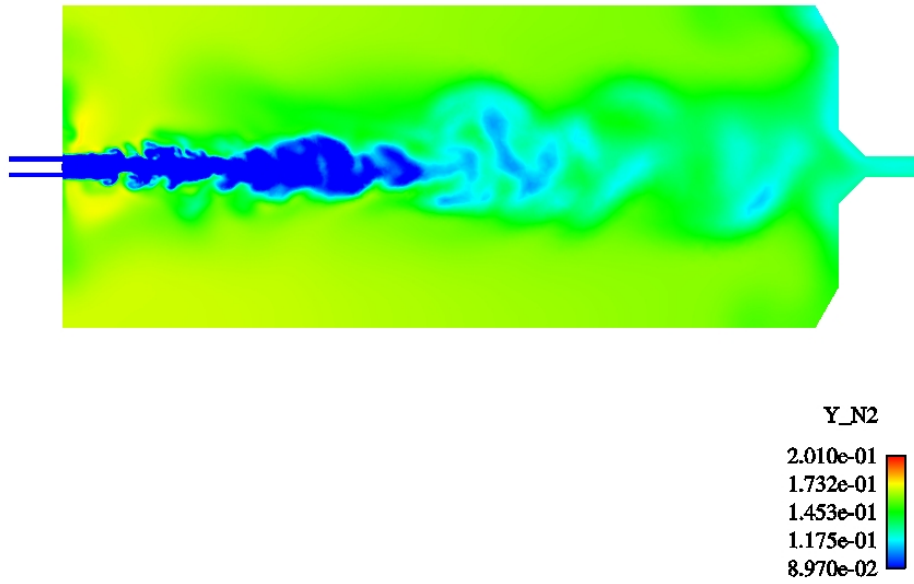2.500e-01
0.000e+00

Figure 4. Oxygen mass fraction at t=370 ms.

Figure 5. Nitrogen mass fraction at t=370 ms.
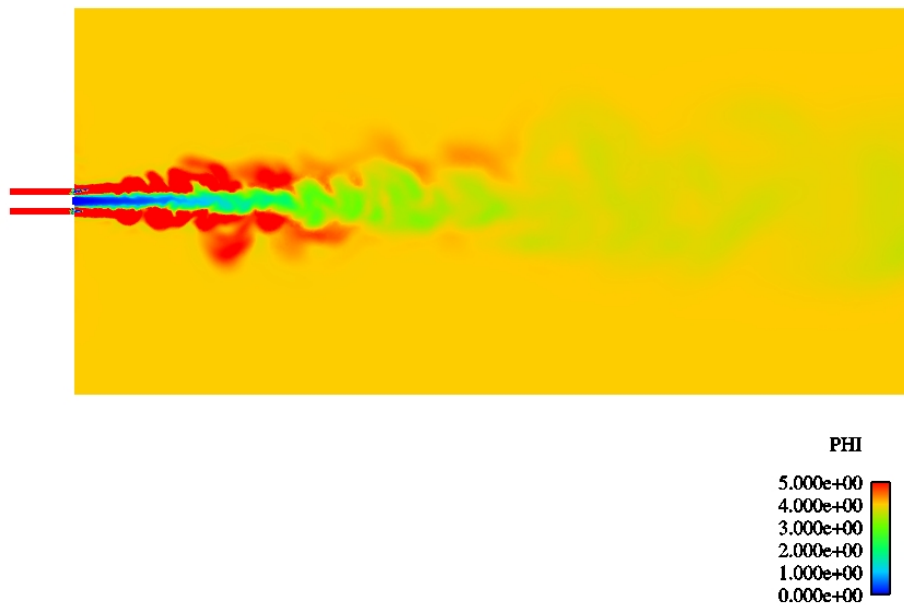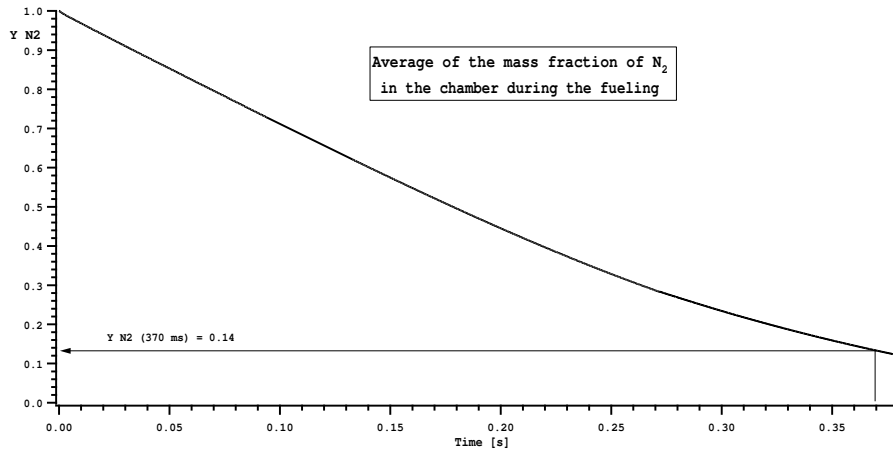

Figure 6. Equivalence ratio at t=370 ms .

Figure 7. Time evolution of the nitrogen in the chamber during the filling phase.
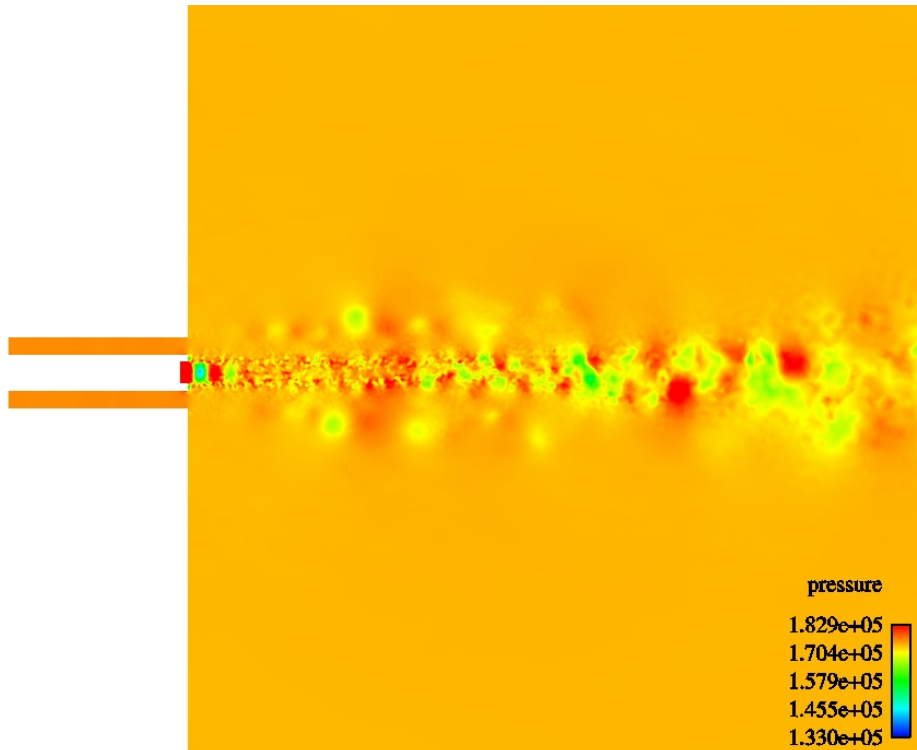
Figure 8. Pressure at t=370 ms (zoom on the injection jets).
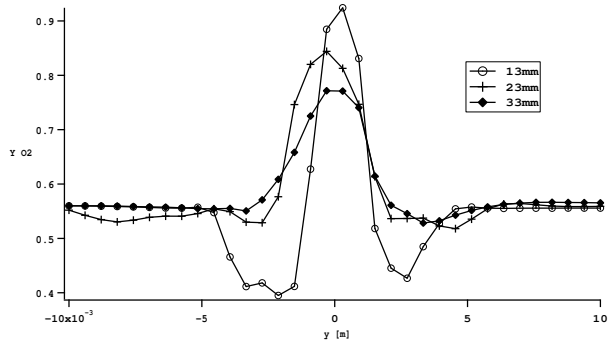
Figure 9. Instantaneous radial profiles of O_2 at different axial locations and at $t = 370ms$.
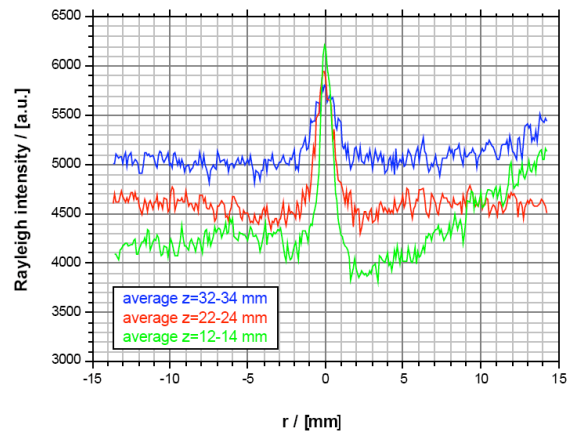
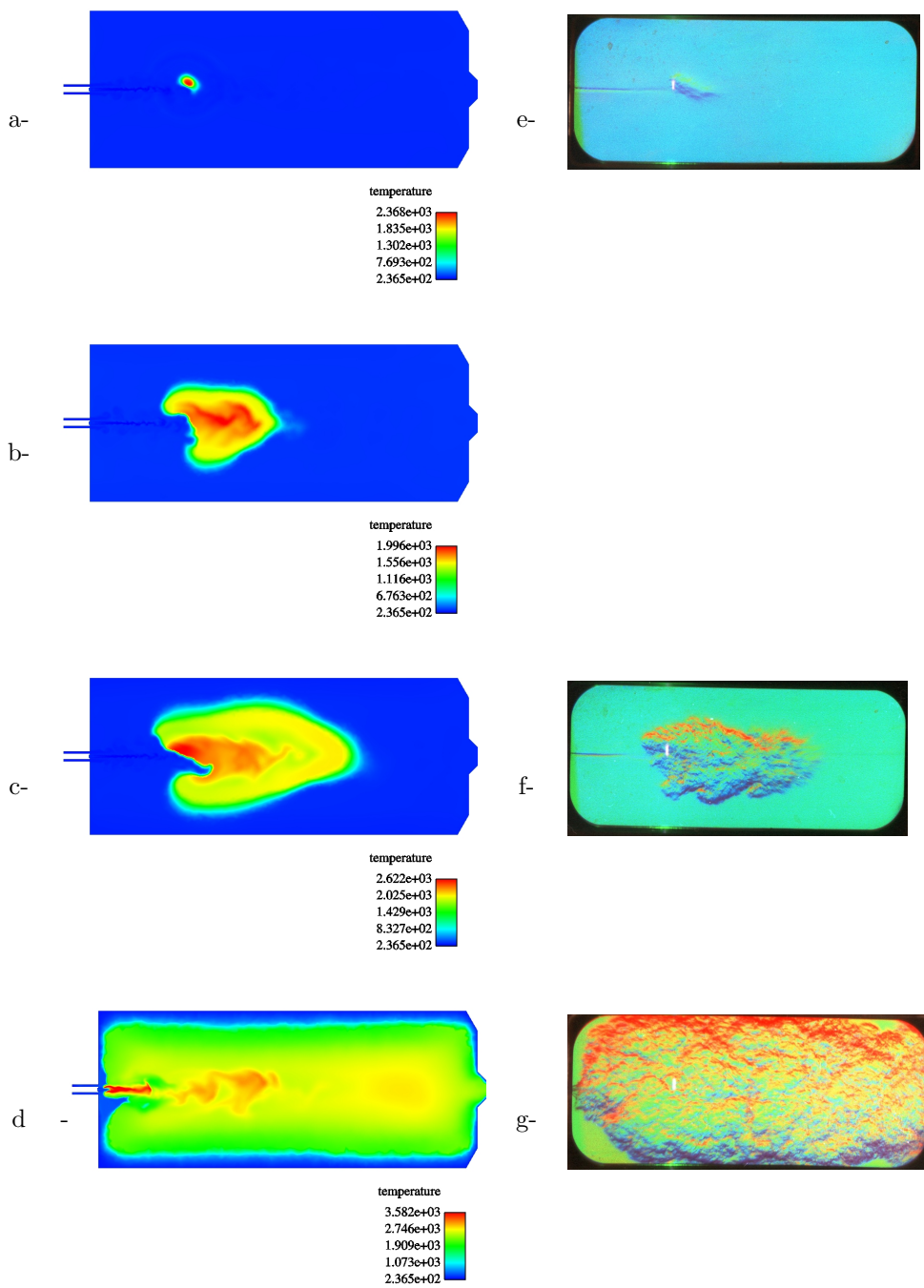**Figure 10. Radial profiles of the Rayleigh intensity at different axial locations**

Figure 11. **Snapshots of the temperature field at four different times after ignition (a:** $t = 15\mu s$**, b:** $t = 103\mu s$**, c:** $t = 226\mu s$**, d:** $t = 684\mu s$**) and Schlieren photographs at three different times after ignition (e:** $t = 35\mu s$**, f:** $t = 250\mu s$**, g:** $t = 680\mu s$**.**
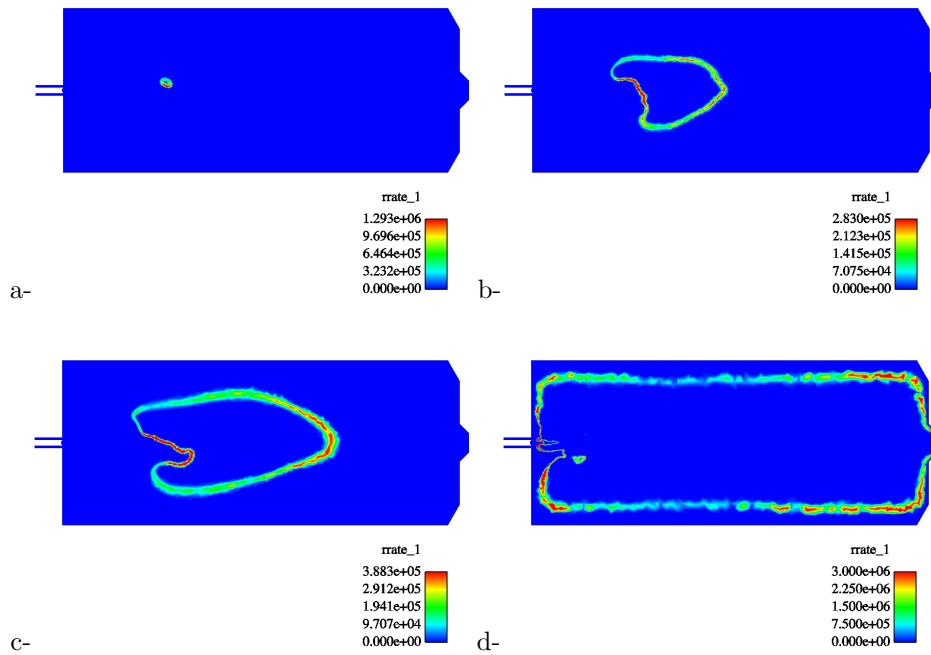
Figure 12. **Snapshots of the reaction rate field at four different times after ignition. a:** $t = 15\mu s$, **b:** $t = 103\mu s$, **c:** $t = 226\mu s$, **d:** $t = 684\mu s$.
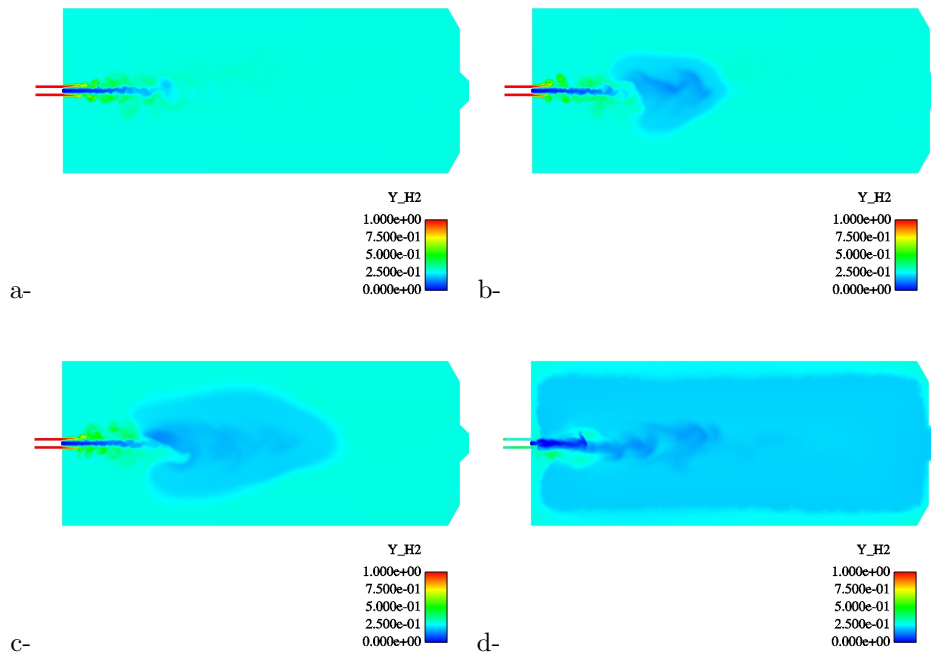

Figure 13. **Snapshots of the hydrogen mass fraction field at four different times after ignition. a:** $t = 15\mu s$, **b:** $t = 103\mu s$, **c:** $t = 226\mu s$, **d:** $t = 684\mu s$.
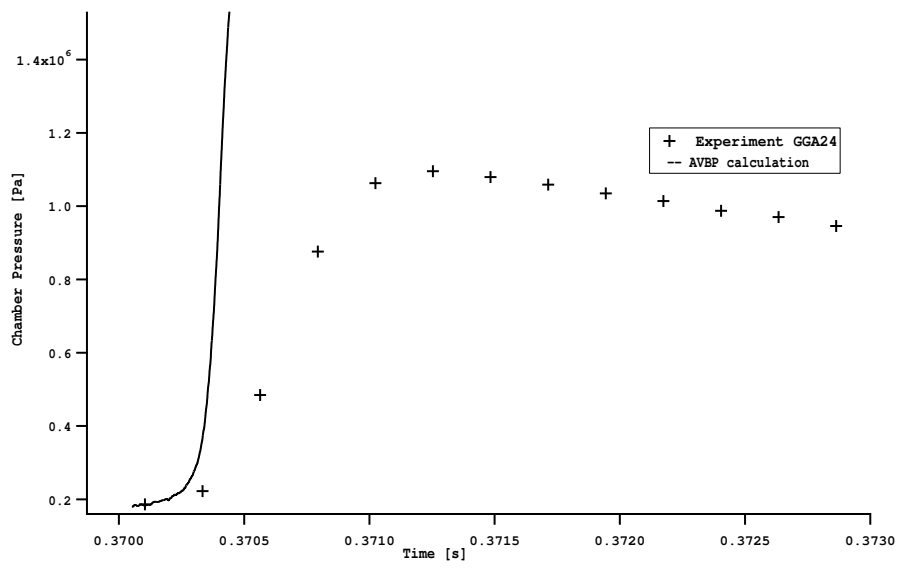
Figure 14.   Local pressure rise in the chamber during the ignition phase.